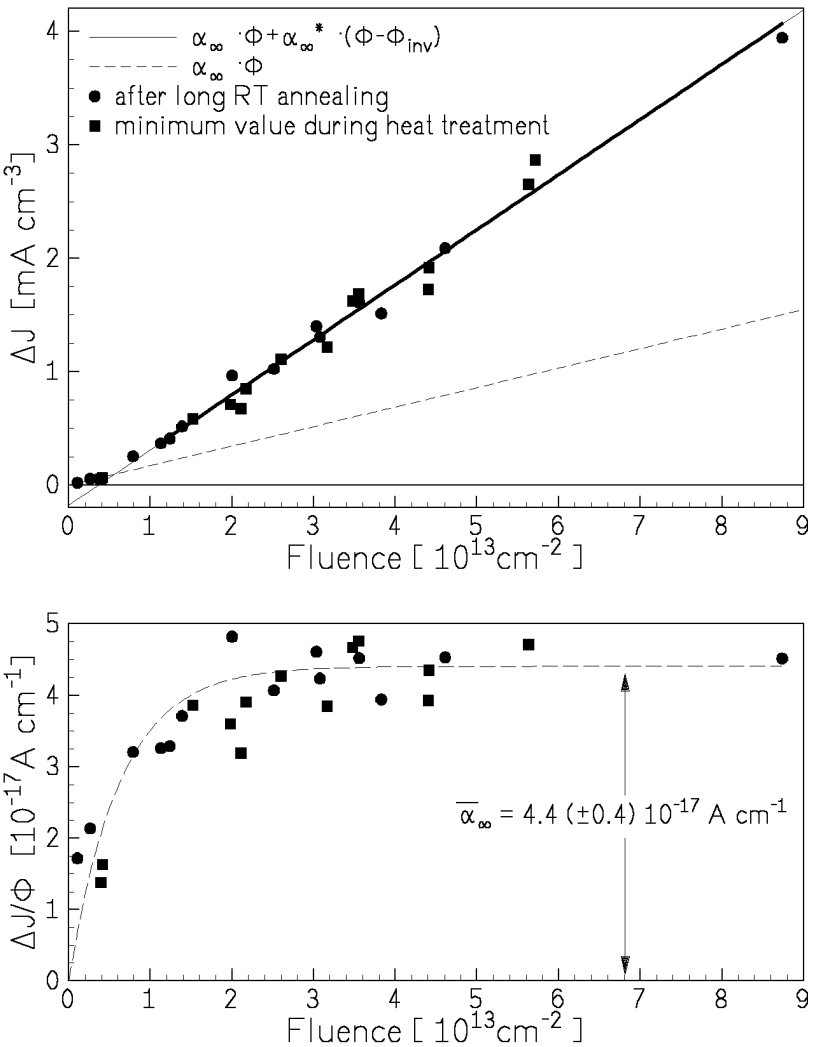

Figure 6.28: Top : Fluence dependence of the reverse current density. Parametrisation according to eq. 6.20. See text for values of α_∞. Bottom : Individual values of ratio $\Delta J/\Phi$ versus fluence. The broken line guides the eye.

6.2.3 Time Dependence at Room Temperature and during the Heat Treatments

The reverse current normalised to volume and fluence of various samples as function of time is shown in fig. 6.29. From a certain time on ($t > 2{\cdot}10^3$ min) the annealing curves are rather similar, the only difference is an individual offset. Furthermore it is evident that after $2{\cdot}10^5$ min ($\approx$ 4 months) a constant value is reached which has been introduced as $\Delta J_\infty/\Phi$ in the last section (sec. 6.2.2). This is in contrast to the effective doping concentration which increases significantly even at room temperature after a minimum value has reached at about half a month. This reverse annealing has been described comprehensively in sec. 6.1.2.

Comparing the data and the annealing curve calculated from the annealing parameters given in tab. 6.8 it becomes obvious that the time constants τ_3 and τ_4 are

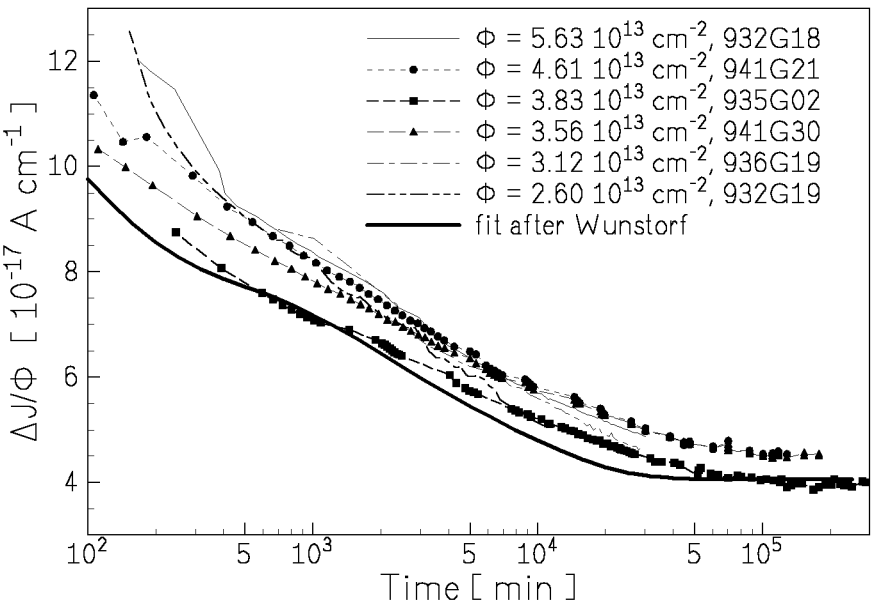

Figure 6.29: Time dependence of reverse current per volume and fluence. Curves which stop at $3 \cdot 10^4$ min are from samples used for the heat treatments (see sec. 6.1). The fit is calculated according to the parameters for inverted material given in tab. 6.8.

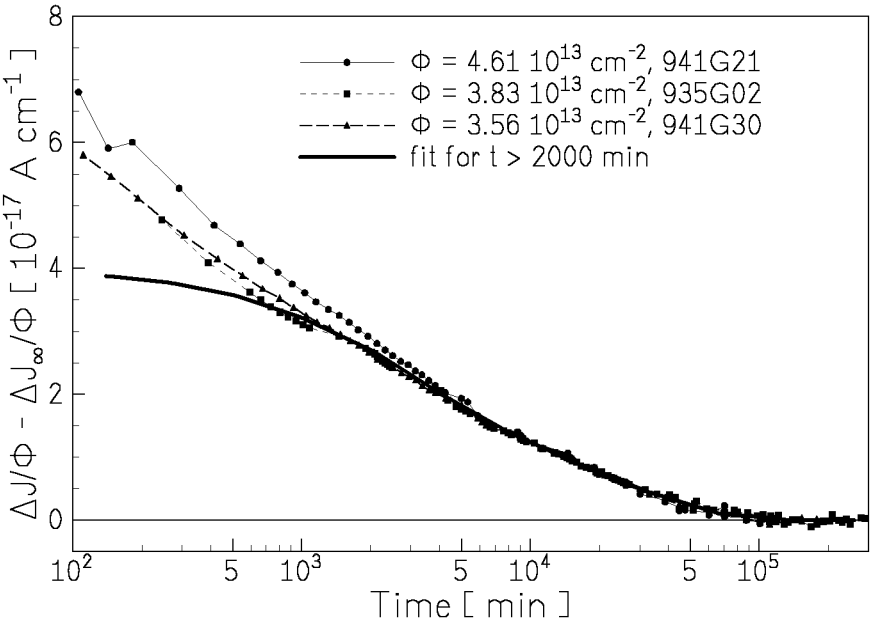

Figure 6.30: Fitted time dependence of current density per fluence. Individual offsets were subtracted. Only those curves were fitted which reached the saturation value. The results of the fit $(\tau_I, \tau_{II}, a_I, a_{II})$ are given in the text.

too short. Hence new time constants were fitted to the data for $t > 2000$ min which is the range of interest for long term prediction. As shown in fig. 6.30 a sum of two exponential functions fits the annealing data very well, if the individual offsets $\Delta J_\infty/\Phi$ are subtracted before. The following time constants and amplitudes were found :

$$\begin{aligned} \tau_I &= 2.65 \cdot 10^3 \text{ min}, \quad a_I = 2.154 \cdot 10^{-17} \text{ A cm}^{-1} \text{ and} \\ \tau_{II} &= 2.30 \cdot 10^4 \text{ min}, \quad a_{II} = 1.840 \cdot 10^{-17} \text{ A cm}^{-1}, \end{aligned}$$

according to :

$$\frac{\Delta J(t)}{\Phi} - \frac{\Delta J_\infty}{\Phi} = a_I * \exp(-t/\tau_I) + a_{II} * \exp(-t/\tau_{II}). \tag{6.23}$$

The error in time constants and amplitudes is about 5%. As expected both time constants are longer than the corresponding numbers given in tab. 6.8. However the ratio of the amplitudes is roughly the same in both cases :
$A_3 : A_4 : A_5 \approx a_I : a_{II} : \Delta J_\infty/\Phi \approx 1 : 1 : 2$.

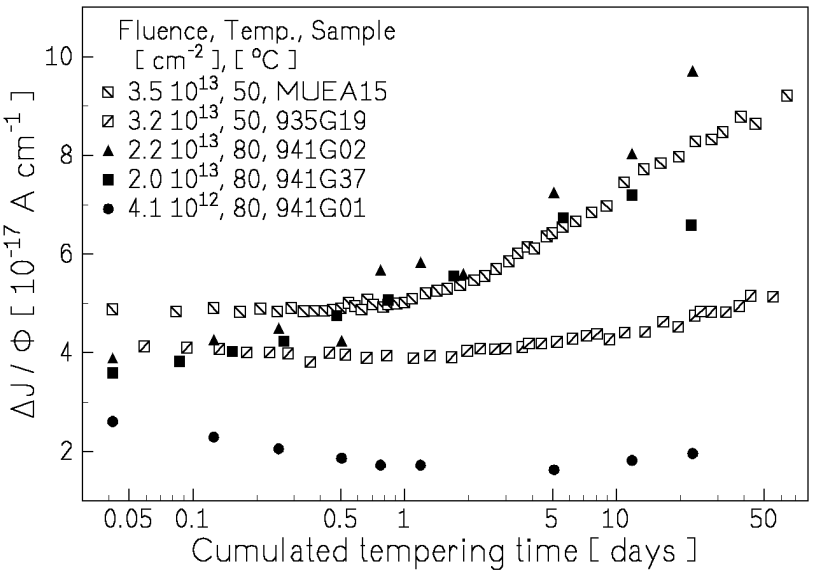

Figure 6.31: Current annealing during heat treatments.

A less conclusive picture emerges from the annealing behaviour at higher temperatures. In fig. 6.31 annealing curves measured at different temperatures are compared. In some cases in a short time range at the beginning of the heat treatments a decrease of the current can be observed, but finally in all cases the current increases with tempering time. Note, that this applies also for the low irradiated sample (941G01). Apparently the annealing behaviour can not be described in a simple way as fluence dependent or normalised to the volume. Hence, it has to be assumed that the change of current during the heat treatments is not caused by generation centres in the bulk. It is conceivable, that surface and interface properties are affected by the heat treatments which cause the rise of the current.

The annealing parameters as determined by Wunstorf [36] are different for not inverted and inverted material. Hence the annealing behaviour has to depend either on the fluence in a general way or on the conduction type of the material. In the first case the parameters for not inverted material should also match for low irradiated p-type material, otherwise the parameters for the inverted material will give a correct description even in the case of low fluence for p-type. In order to decide experimentally between both possibilities p- and n-type detectors were irradiated with low and high fluences, $3{\cdot}10^{12}$ cm^{-2} and $4{\cdot}10^{13}$ cm^{-2} respectively. Fig. 6.32 shows the subsequent annealing of the reverse current normalised to volume and fluence. The difference of n- and p-type annealing can be seen very clearly in the time range 500 to 5000 min. The curves of both p-type samples and the inverted one coincide after shifting them along the y-axis, i.e. subtracting components of the current that do not change in time. It is evident that the annealing curve of the low irradiated n-type sample will not match the p-type curves whatever is added or subtracted.

Thus, it can be concluded that the conduction type of the material has a significant meaning on the current annealing behaviour.

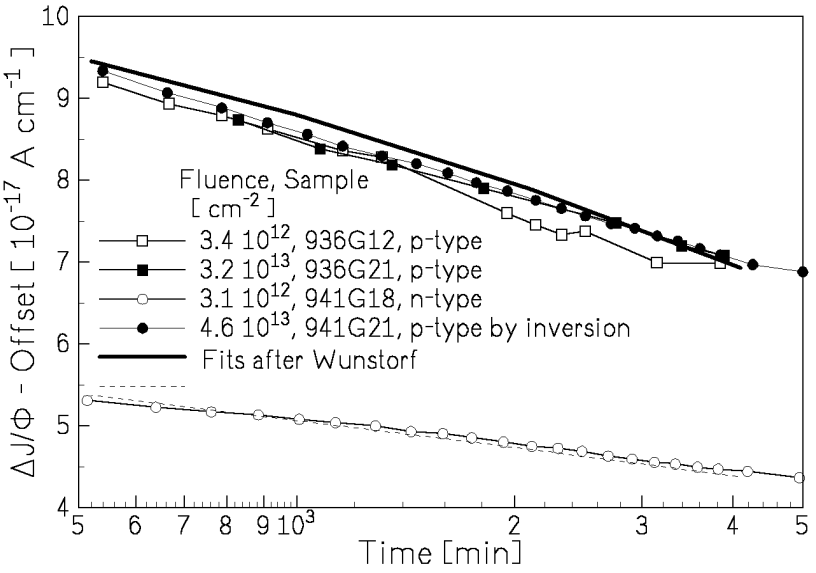

Figure 6.32: Comparison of current annealing in p- and n-type material.

6.2.4 Annealing at Lower Temperature

The annealing behaviour at lower temperature has been investigated using 3 sets of different samples. Each set consisted of one SB-detector and two p^+-n -detectors from *Micron* and *Intertechnique* which were irradiated and afterwards stored at the same temperature. The temperatures were 6°C, 10°C, and 14°C, respectively (see sec. 5.4).

For comparison the current densities ΔJ were normalised to the standard temperature $T = 20°C$ using eq. 4.6 :

$$\Delta J_{20} = RT(T)\Delta J(T) \tag{6.24}$$

The data of the samples and the applied factors $RT(T)$ are listed in tab. 6.9.

Samples in a Set			Φ $[10^{13} cm^{-2}]$	T [°C]	$RT(T)$
932G20	MUEA24	INTA06	2.75	14	1.72
932G04	MUEA22	INTA19	2.75	10	2.50
937G30	MUEA23	INTA21	2.95	6	3.67
	MUEA15		3.51	21	0.92

Table 6.9: Parameters of samples for current annealing at low temperature. The room temperature annealing curve of sample MUEA15 is used for comparison and hence the corresponding data are also listed here.

In fig. 6.33 the normalised current densities are plotted versus time. It can be seen that the current densities of the Intertechnique detectors are always the highest, at least in the time range up to $5 \cdot 10^4$ min. The current voltage characteristics of these samples do not obey the $\sqrt{V}$-dependence, but show a stronger current increase which is assumed to be caused by surface effects. [7]

Vice versa the current densities of the SB-detectors are lower at 6°C and 14°C.[8] This may be caused by the different fabrication technologies. But it is also possible that the volume of the p^+-n -detectors is under-estimated, because no lateral extension of the electrodes effective area has been taken into account. An under-estimated volume leads to an over-estimated value of ΔJ. If e.g. the currents of the Micron samples and the SB-detectors are compared at about 4000 min, the ratio is found to be 1.3 in both cases (see also sec. 7.1.4). A ratio of 1 can be achieved if the effective area of the p^+-n -samples is estimated by A = 0.33 cm^2 instead of 0.25 cm^2. However, the same value should apply for the Intertechnique samples, but as mentioned above it does not. Thus the volume of the p^+-n -detectors has been calculated using the geometrical area of the electrode A = 0.25 cm^2.

Comparing the normalised currents I_{20} of one type of sample (e.g. Micron) at different temperatures but same times, it is found that with decreasing temperature the current increases. This is a consequence of a higher defect concentration at lower temperatures. The amount of defects generated per fluence can be regarded as independent of the temperature. But as described in sec. 3.2 the annealing process is rather temperature dependent and defects which anneal out very rapidly at room temperature may contribute to the bulk generation current for a much longer time at a lower temperature. It must be emphasised however, that in the temperature range under discussion for the measured currents still holds : $I(T_1) < I(T_2)$, if $T_1 < T_2$.

[7] The different passivations used for these samples could be responsible. However, in-between Intertechnique has changed the fabrication process and thus the problem is solved.

[8] The current voltage characteristics of the sample 932G04 ($T = 10°C$) could not be analysed.

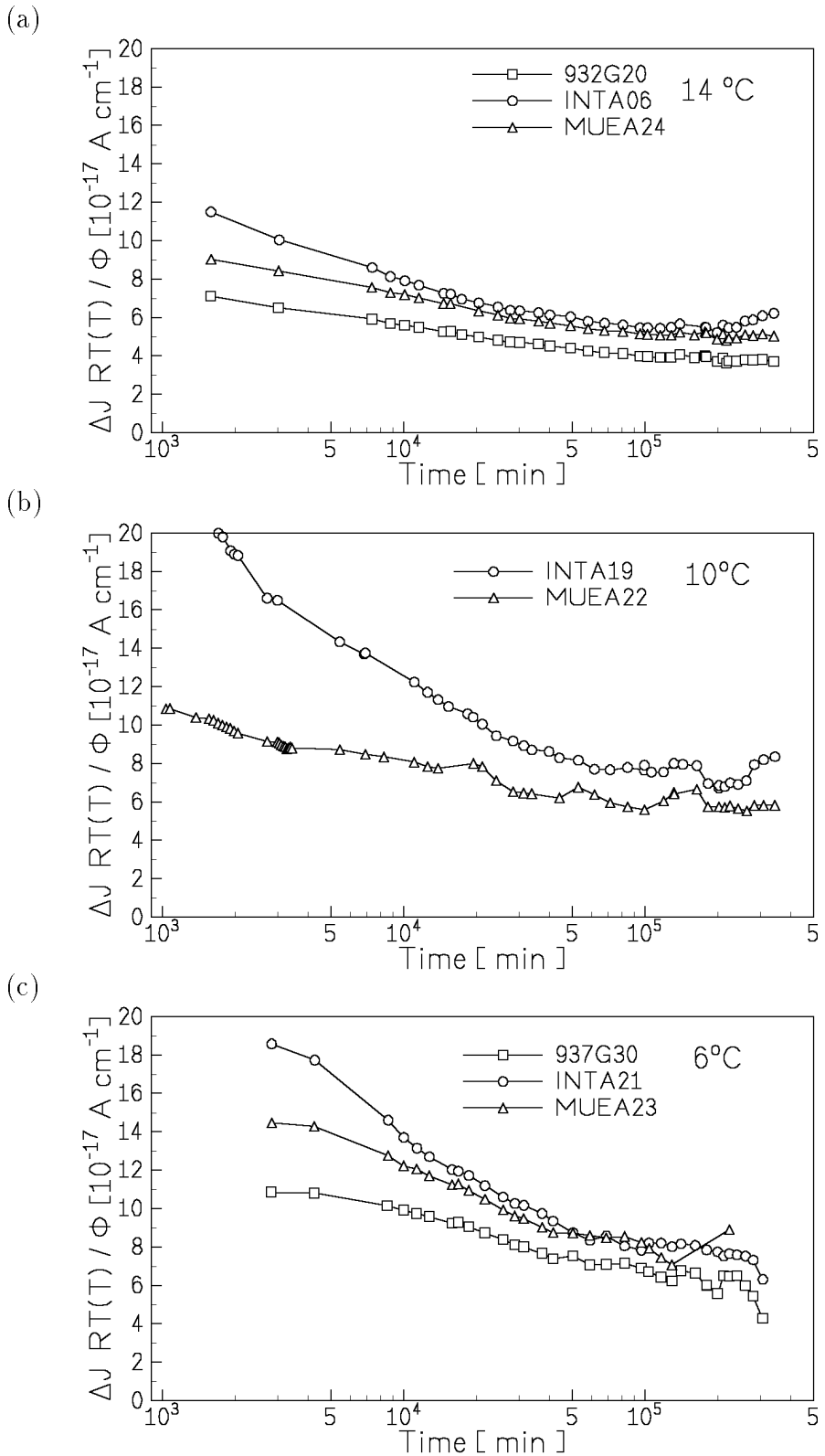

Figure 6.33: Current annealing at 14°C (a), 10°C (b), and 6°C (c).

Each annealing curve has been analysed in order to obtain a set of amplitudes and time constants as already used to describe the room temperature annealing of the reverse current. Again the short term annealing has not been considered, because it happened in a time range similar to the exposure time itself. The results are listed in tab. 6.10.

Sample	T [°C]	$\Delta J_\infty/\Phi$ $[10^{-17}\frac{A}{cm}]$	a_{II} $[10^{-17}\frac{A}{cm}]$	τ_{II} $[10^4$ min$]$	a_I $[10^{-17}\frac{A}{cm}]$	τ_I $[10^3$ min$]$
INTA21	6	6.97	2.07	25.8	8.67	19.8
INTA21	10	6.81	2.00	10.8	8.88	12.0
INTA06	14	5.36	2.23	4.02	5.10	5.71
MUEA22	10	5.55	1.55	7.38	2.61	12.9
MUEA24	14	5.01	2.13	3.63	2.48	6.86
932G20	14	3.74	1.76	4.51	1.91	6.57
see caption	20	4.40	1.84	2.30	2.15	2.65

Table 6.10: Individual annealing parameters. No data are listed if the time constants could not be separated. The 20°C-data were obtained in the preceding section as an average value of a few room temperature annealing curves.

The 2 : 1 : 1-ratio which was found for the room temperature annealing in the preceding section, applies for none of the Intertechnique sample and especially a_I and the non-annealing fraction are significantly greater than the values obtained for the Micron and SB-samples respectively. The difference of the amplitudes between these two types can be explained again if the effective area of the Micron sample is assumed to be larger than the geometrical. Considering also the possible surface effects of the Intertechnique samples it becomes obvious that as expected the non-annealing fraction is independent of the temperature.

The time constants listed in tab. 6.10 are also plotted in fig. 6.34. From the Arrhenius relation the activation energies of the corresponding annealing processes are determined :

$$\begin{aligned} E_{aI} &= 0.99\ (\pm\ 0.1)\ \text{eV and} \\ E_{aII} &= 1.16\ (\pm\ 0.1)\ \text{eV}. \end{aligned}$$

Although the time constants differ by an order of magnitude the activation energies are approximately equal. This is due to the different pre-factors :

$$\begin{aligned} 1/\tau_{0,I} &= \hat{k}_{0,I} = 2.5{\cdot}10^{15}\ \text{s}^{-1}\ \text{and} \\ 1/\tau_{0,II} &= \hat{k}_{0,II} = 3.0{\cdot}10^{17}\ \text{s}^{-1}. \end{aligned}$$

Both $\tau_{0,I}$ and $\tau_{0,II}$ can not be associated with the most abundant phonon frequency (10^{13} s^{-1}). However, the experimental values are only 2 or 4 orders of magnitude higher than the estimate of $\hat{k}_0$, instead of 8 orders as found for $\hat{k}_0$ from the reverse annealing parametrisation in sec. 6.1.2.7.

The similarity of the activation energies allows the calculation of the temperature dependent delay of the annealing process in a very simple way. Scaling an annealing

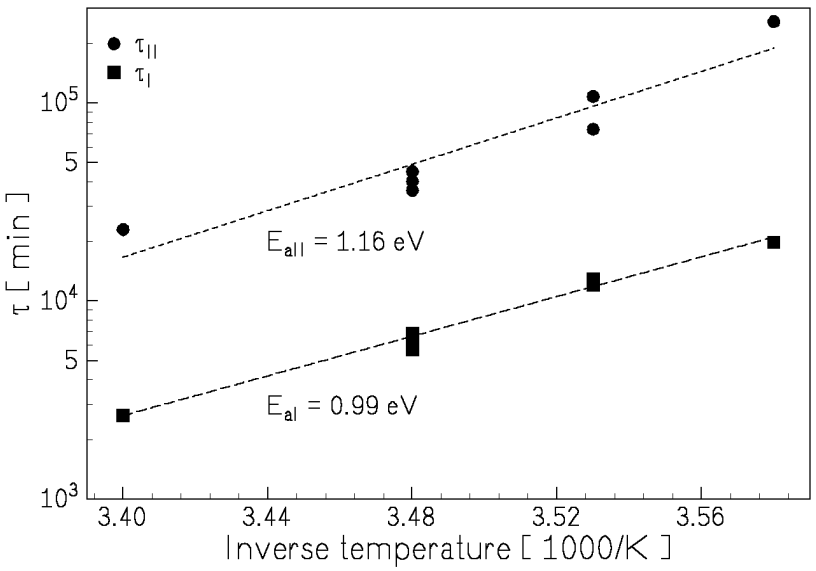

Figure 6.34: Time constants of annealing stages I and II versus inverse temperature.

curve measured at temperature T by a factor $\theta(T)$ it matches the room temperature annealing curve. The scaling factor can be calculated according to:

$$\theta(T) = \exp\left(\frac{E_a}{k_B}\left(\frac{1}{293.16} - \frac{1}{T}\right)\right). \tag{6.25}$$

This is demonstrated in fig. 6.35. Figure (a) shows annealing curves measured at different temperatures. For comparison only Micron samples are used and a room temperature annealing curve has been added. The same annealing curves are shown in figure (b), but scaled by a factor $\theta(T)$ and after subtraction of the non-annealing fraction. The scaling factor is calculated using eq. 6.25 and an activation energy $E_a = 1.08$ eV which is the average value of $E_{a,I}$ and $E_{a,II}$. It can be seen that the annealing curves do not coincide completely. This indicates that the subtracted offsets which resulted from a fit are incorrect. The scaling factor has been used already by Chilingarov [124], who found a rather similar activation energy (1.09 eV) in a more pragmatic way.

6.3 Comparison of Current and N_{eff} Related Results

The effective doping concentration and the reverse current have been investigated with respect to the annealing behaviour at different temperatures and the fluence dependence of the corresponding damage which occurs in the long time range. Both quantities are found to increase linearily (but not in proportion) with fluence after type inversion. In the fluence range below type inversion the effective doping concentration is governed by the donor removal and the reverse current increases indeed in proportion with the fluence.

a)

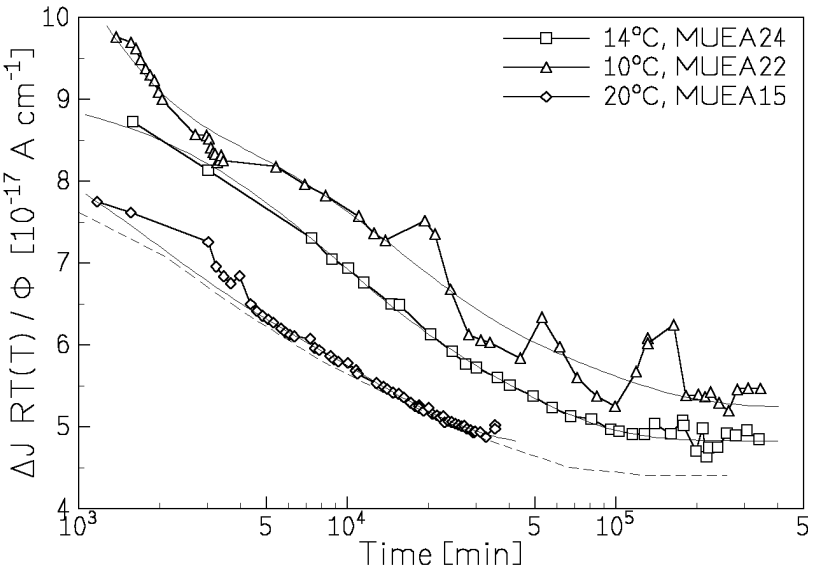

b)

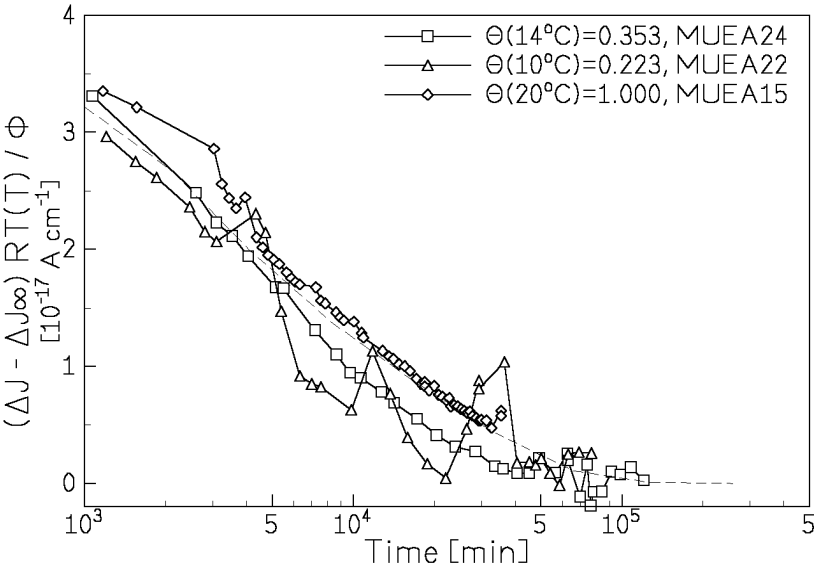

Figure 6.35: Annealing of reverse current at different temperatures. Solid lines are individual fits, broken lines present fits according to eq. 6.23 and corresponding parameters. Annealing of reverse current at different temperatures scaled by $\theta(T)$ (see eq. 6.25)

The short term annealing behaviour of both quantities is comparable only in the time range below $t \approx 5{\cdot}10^5$ min. The amplitudes and time constants which were found to parametrise the annealing are compiled in tab. 6.11. The 'short' as well as

No.	Eff. Dop. Conc.		Reverse Current	
	Time Constant τ [min]	Amplitude b [cm^{-1}]	Time Constant τ [min]	Amplitude a [10^{-17} A cm^{-1}]
I	$1.80{\cdot}10^3$	0.015	$2.65{\cdot}10^3$	2.15
II	$1.84{\cdot}10^4$	0.0075	$2.30{\cdot}10^4$	1.84
	∞	r.a. $*$	∞	4.40 $\star$

Table 6.11: Comparison of annealing parameters of the effective doping concentration and the reverse current. $*$: reverse annealing, $\star$: average value.

the 'long' time constant of current and N_{eff} annealing are rather similar and have a ratio of 10 in both cases. In contrast the amplitudes differ by a factor of 2 in case of the effective doping concentration and are approximately equal in case of the current. Nevertheless, according to the issues discussed in sec. 3.4 (p.36) a direct correlation of both quantities is possible. From eqs. 3.15 and 3.18 it follows, that

$$I_{BGC} = q\,AW\,N_T f_T\,e_n. \tag{6.26}$$

The fraction of occupied centres will contribute to the space charge concentration (see also eq. 3.20) :

$$N_{SC} = N_T f_T. \tag{6.27}$$

Combining eqs. 6.26 and 6.27 it follows :

$$N_{SC} = \frac{I_{BGC}}{q\,AW\,e_n} = \frac{J}{qe_n}. \tag{6.28}$$

It can be seen that the contribution of the generation centres to the effective space charge is governed by the emission rate. For a given current a small rate results in a stronger contribution and vice versa a great rate will result in a lower contribution. Because both the current and the space charge amplitudes grow in proportion to the fluence N_{SC} can be replaced by $b \cdot \Phi$ and J/q by $a \cdot \Phi$. Thus the emission rate of the corresponding defect-level can be expressed in terms of b and a :

$$\frac{1}{e_n} = \frac{b}{a}q. \tag{6.29}$$

Applying this equation to the amplitudes listed in tab. 6.11 one obtains the following emission rates :

$$e_{n,I} = \frac{a_I}{b_I\,q} \approx 9 \cdot 10^3 s^{-1}, \tag{6.30}$$

$$e_{n,II} = \frac{a_{II}}{b_{II}\,q} \approx 15 \cdot 10^3 s^{-1}, \tag{6.31}$$

which will be compared to the values determined by DLTS (see sec. 7.3).

Very different from the short term behaviour is the long term annealing, because current and space charge undergo different developments. The current is found to remain constant in time, while the effective doping concentration increases again. Thus it can be definitely excluded that the defects generated during the reverse annealing are correlated with the current. However, it is possible that the part of the space charge which is constant in time and proportional to the fluence $(N_C - N_{C,0})$ (see eq. 6.13) may be correlated with current as suggested already for the annealing components. Eq. 6.29 leads to :

$$e_{n,\infty} = \frac{\overline{\alpha_\infty}}{b_C\, q} \approx 16 \cdot 10^3 s^{-1}, \tag{6.32}$$

a value being very similar to the one obtained for the annealing component II. The corresponding pairs of ΔE_T and σ have reasonable values. If e.g. a mid-gap centre with $\Delta E_T = 0.56$ eV is assumed, the corresponding cross section is about 10^{-13} cm^2. For a smaller energy value also the cross section becomes smaller (see eq. 2.42).

Nevertheless the correlation of current and space charge as suggested in this section is not cogent. But it is justified by the similarity of the annealing time constants. Furthermore it is rather unlikely that the generation centres do not contribute to the space charge in any way.

The annealing of the current and effective space charge at lower temperature is slowed down. In case of the current still two components are found, and the corresponding time constants behave as expected from the Arrhenius relation. In contrast the annealing of the space charge is less differentiated. The time constants at different temperatures are equal. The suggestion of current - space charge relation is weakened by this finding.

At elevated temperature the development of the space charge is dominated (exclusively) by the reverse annealing. No consistent description could be found for the annealing of the current at elevated temperature.

Chapter 7

Defect Characterisation

7.1 Deep Level Transient Spectroscopy

7.1.1 Introduction

A DLT-spectrum of a n-type SB-diode after neutron irradiation shows up to 7 positive peaks which correspond with electron traps. The peaks are labelled E1 - E7. The detection of hole traps is not possible because the majority carriers are electrons, and even the forward current bases on the majority carriers (see sec. 4.1.2). For example a spectrum is shown in fig. 7.1.

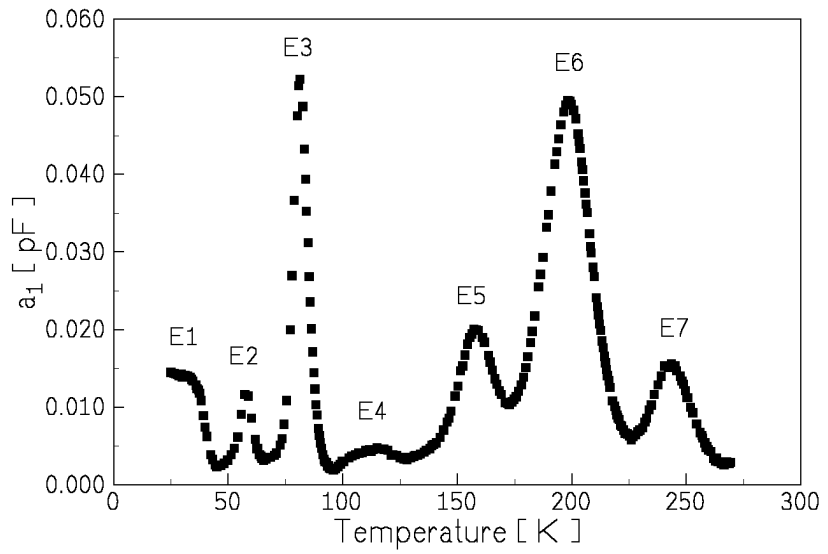

Figure 7.1: Characteristic spectrum after irradiation of a n-type SB-diode. (911G21, $\Phi = 4.5 \cdot 10^{10}$ cm^{-2}).

In the following some properties of the peaks are discussed briefly. The given temperatures of peak maximum T_m are determined from the measurement shown in fig. 7.1 which was performed with a time window $t_w = 50$ ms. In the spectra shown